

PKS2250-41: a case study for triggering^{*}

K. J. Inskip^{1†}, M. Villar-Martín², C. N. Tadhunter¹, R. Morganti³, J. Holt^{1,4} and D. Dicken¹

¹ *Department of Physics & Astronomy, University of Sheffield, Sheffield S3 7RH*

² *Instituto de Astrofísica de Andalucía (CSIC), Aptd0. 3004, 18080 Granada, Spain*

³ *Netherlands Foundation for Research in Astronomy, Postbus 2, 7990 AA Dwingeloo, The Netherlands*

⁴ *Sterrewacht Leiden, Postbus 9513, 2300 RA Leiden, The Netherlands*

ABSTRACT

We present the results of a multiwavelength study of the $z = 0.31$ radio source PKS2250-41. Integral field unit and long-slit spectroscopy obtained using VIMOS and FORS1 on the VLT, and archival HST optical imaging observations are used to study the morphology, kinematics and ionisation state of the extended emission line region (EELR) surrounding this source, and also a companion galaxy at a similar redshift. Near-infrared imaging observations obtained using the NTT are used to analyse the underlying galaxy morphologies. The EELR displays a complex variety of different gas kinematics and ionization states, consistent with a mixture of radio source shocks and AGN photoionization.

The radio galaxy is likely to lie within a group environment, and is plausibly undergoing interactions with one or more other objects. The disk-like galaxy to the northeast of the radio source lies at a similar redshift to the radio galaxy itself, and has its major axis position angle aligned with the filamentary continuum and line emission extending outwards from the radio galaxy. This filamentary structure is most plausibly interpreted as a tidal structure associated with an interaction involving the radio source host galaxy and the aligned companion galaxy to the north-east; this encounter may have potentially triggered the current epoch of radio source activity. Overall, PKS2250-41 displays some of the best evidence that radio source activity can be triggered in this manner.

While the environment and recent interactions of a radio galaxy can have some bearing on its subsequent evolution, our data also highlight the varied means by which the radio source can effect changes in adjacent objects. Our IFU and long-slit spectroscopy confirm the presence of radio source shocks within the western radio lobe, and, together with our continuum observations, add further weight to the presence of a faint continuum source coincident with the secondary hotspot in the western radio lobe. On the basis of our multiwavelength observations of this object, we suggest that the radio source has indeed triggered recent star formation within this faint companion.

Key words: galaxies: active – galaxies: evolution – galaxies: haloes – galaxies: interactions – galaxies: individual: PKS2250-41 – galaxies: ISM

1 INTRODUCTION

The presence of a powerful radio source is known to have profound implications for the properties of both the host galaxy and the surrounding intergalactic medium (IGM).

While the host galaxies are usually massive ellipticals with predominantly old stellar populations formed at $z \sim 5 - 20$ (e.g. Inskip et al 2002a), increasing evidence is accumulating for more recent star formation in many sources (e.g. Wills et al 2007, Holt et al 2007 and references therein). Extended emission line regions (EELRs) are frequently observed around radio galaxies (McCarthy et al 1987), and their observed properties (size, luminosity, kinematics and ionisation state) are known to depend strongly on those of the radio source (e.g. Best et al 2000, Inskip et al 2002b,c,

^{*} Based on observations collected at the European Southern Observatory, Chile (programs 071.B-0320(A), 074.B-0310(A), 075.B-0820(A) and 078.B-0500(A))

[†] E-mail: K.Inskip@shef.ac.uk

Moy & Rocca-Volmerange 2002, Humphrey et al 2006). However, the origin of the emitting material is less well understood. Overall, disentangling cause from effect within these complex systems is far from straightforward; which properties are genuine symptoms of the radio source activity, and which can be tied to the underlying AGN triggering mechanism?

Integral field spectroscopy (IFS) provides a powerful tool for addressing questions such as these. The additional spatial data provided by IFS observations is a major advantage, as it allows the EELR properties (physical conditions, gas dynamics, ionisation state) to be efficiently studied and quantified as a function of position relative to the radio source, rather than just along the radio axis, as is commonly the case for most long-slit spectroscopic studies. In this paper, we consider the case of the $z \sim 0.31$ radio galaxy PKS2250-41, previous observations of which have shown it to be surrounded by one of the most impressive EELRs identified at intermediate redshifts (Tadhunter et al 1994; Clark et al 1997; Villar-Martín et al 1999). We present the results of a multi-wavelength study of this source, combining optical IFS spectroscopy, optical long-slit spectroscopy, near-IR imaging and optical continuum and emission line imaging.

The details of the source, our observations and data reduction are described in section 2, and the results presented in section 3, including an analysis of potential companion objects at a similar redshift. In section 4, we discuss the implications of our results, and we present our conclusions in section 5. Throughout this paper, we assume cosmological parameters of $\Omega_0 = 0.3$, $\Omega_\Lambda = 0.7$ and $H_0 = 70 \text{ km s}^{-1} \text{ Mpc}^{-1}$, which result in an angular scale of $\sim 4.55 \text{ kpc/arcsec}$ at $z \sim 0.31$.

2 SOURCE DETAILS, OBSERVATIONS AND DATA REDUCTION

2.1 Source details

PKS2250-41 is an FR II radio source hosted by an elliptical galaxy lying at a redshift of $z = 0.308$, and a member of the large sample of southern 2Jy sources selected for study by Morganti, Killeen and Tadhunter (1993) and Tadhunter et al (1993). Fig. 1 displays the most recent optical and infrared imaging of this source, overlaid with VLA radio contours.

The EELR surrounding PKS2250-41 is particularly striking, and has been well-studied in the past. Imaging, spectroscopic and polarimetric observations of this source were obtained in 1993, and the results presented in a number of papers (Tadhunter et al 1994, Shaw et al 1995 and Clark et al 1997). The major feature of this source is the bright emission line arc lying approximately 5.5 arcsec west of the host galaxy, circumscribing the radio lobe, with lower surface brightness line emission lying to the east of the host galaxy. The varied gas kinematics and ionization states observed in the western arc provide some of the best evidence in any active galaxy for the presence of shocked gas with a photoionized precursor region, plausibly caused by jet-cloud interactions. Emission line density and temperature diagnostics imply high pressures in the western radio lobe, suggesting pressure equilibrium within this region. After subtraction of the nebular continuum emission from this region, Dickson et

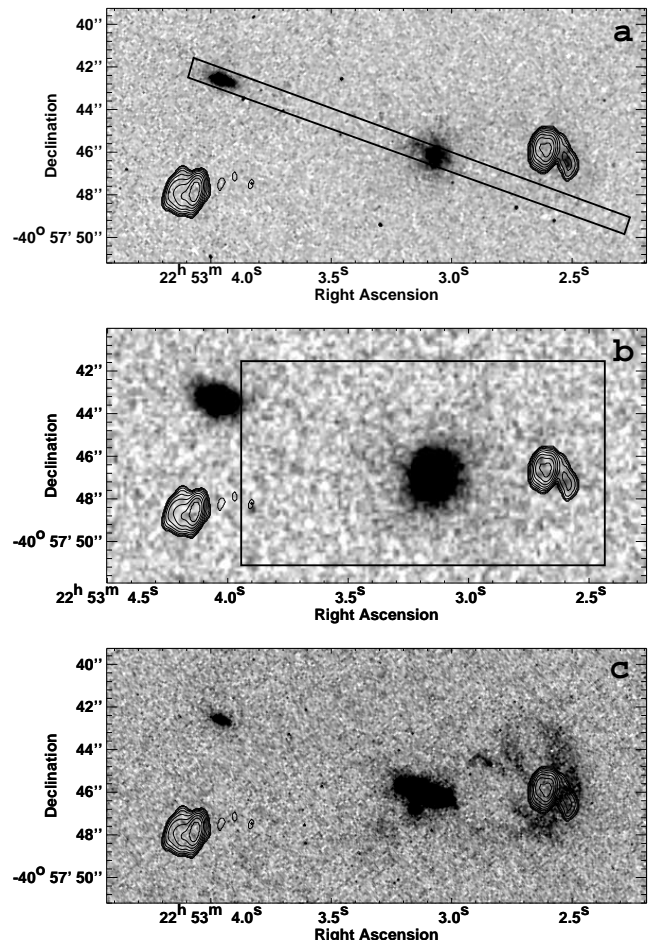


Figure 1. (a - top) Optical WFPC2 F547M image of PKS2250-41, overlaid with 15GHz VLA radio contours, also illustrating the location of the PA 69° $1.3''$ FORS1 slit. (b - centre) Infrared SOFI Ks image of PKS2250-41, overlaid with 15GHz VLA radio contours, also illustrating the region of the VIMOS IFU field of view studied in detail in this paper. (c - bottom) WFPC2 [OIII]5007Å emission line image of PKS2250-41, overlaid with 15GHz VLA radio contours. The WFPC2 and radio data are taken from T05. The major features to note in frame (c) are the extensive emission line arc to the west, coincident with the radio emission in the western lobe, and a bright linear structure running NE-SW across the host galaxy, aligned towards the companion galaxy to the NE.

al (1995) found that the remaining continuum is relatively blue in colour, while Shaw et al (1995) showed that it is also unpolarised. Clark et al (1997) hypothesise that the western arc originates from a direct collision between the radio jet and a companion object. They also suggest that the galaxy lying at a distance of approximately 10.5 arcsec/50 kpc to the northeast of PKS2250-41 lies at a similar redshift to the radio source and that the two galaxies may be undergoing some level of interaction. It should be noted that their data were of lower signal-to-noise, and were not definitive with regard to the redshift of the companion.

On the basis of the clear evidence for jet-cloud interactions displayed by this source, Villar-Martín et al (1999; hereafter VM99) carried out a further, higher resolution spectroscopic study utilising four different slit positions,

Table 1. Details of the observational data used in this paper. The listed seeing measurements are given for the wavelength of the observations in question.

Date	Instrument	Time (s)	Seeing	Notes
2003/07/24	FORS1	6720	0.4-0.7''	polarimetry
2004/10/19	VIMOS	13560	1.1-1.5''	cirrus
2004/11/19	VIMOS	9040	1.1-1.5''	photometric
2005/06/07	VIMOS	17600	0.7-1.1''	photometric
2005/06/09	VIMOS	8800	0.5''	photometric
2006/11/14	SOFI	3000	0.8''	photometric

three aligned on, above and below the host galaxy centroid and parallel to the radio axis, and one perpendicular to the radio source axis, aligned with the western emission-line arc. Two different kinematic components were identified within the gas, and the other emission line properties (temperature, ionization state, ionization mechanism) clarified, adding strong support to the picture of cooling gas behind a shock front driven by the radio jets, as well as a photoionized precursor region.

The subsequent emission-line and continuum imaging of Tilak et al (2005; hereafter T05) is in keeping with this picture. The different ionization states within the arc are spatially and spectrally resolved, suggesting a cooling-region behind the radio source bow-shock. Continuum emission is potentially observed at the location of the secondary hotspot, and a continuum spur extending northeastwards from the host galaxy is identified, aligned with the brightest emission line features in that region.

The observations of PKS2250-41 presented in this paper include optical long-slit and integral field unit spectroscopy, and infrared imaging. The primary goals of these observations are to deepen our understanding of the EELR surrounding this source with regards to its origin, including both the western emission-line arc and the filamentary spur extending towards the northeast, and additionally to investigate the nature of the possible companion galaxies. The observational data presented in this paper is outlined in full in the remainder of this section, with brief details provided in Table 1.

2.2 FORS1 spectroscopic observations

Long-slit spectropolarimetry observations of PKS2250-41 were obtained on 2003 July 24 using the Focal Reducer/low dispersion Spectrograph (FORS1; Appenzeller et al 1998) as part of the European Southern Observatory (ESO) observing programme 071.B-0320(A). FORS1 is mounted on the Nasmyth focus of the UT2 Kueyen unit of the Very Large Telescope (VLT). The instrument was used with the GG435 filter and GRIS_600R grism, giving a spectral resolution of $1.07\text{\AA}/\text{pixel}$, an instrumental resolution of $5.9\pm 0.1\text{\AA}$, a plate scale of $0.2\text{ arcsec}/\text{pixel}$ and an overall observed-frame useful spectral coverage of $\sim 5520 - 7410\text{\AA}$. The slit width during the observations was 1.3 arcsec . Sixteen separate 420s observations were made, in excellent seeing conditions of $0.4\text{-}0.7''$. The position angle of the FORS1 slit was 69° , and is illustrated in Fig. 1, overlaid on a ground-based emission line plus continuum image of PKS2250-41 (Clark et al 1997). In addition to including flux from the host galaxy and a sub-

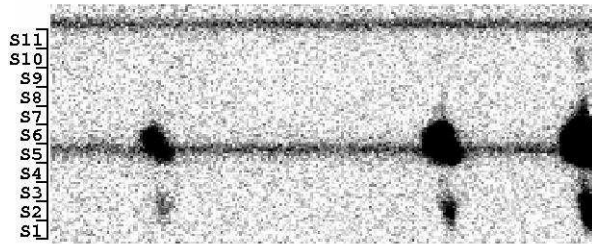


Figure 2. Section from the 2-d FORS1 spectrum of PKS2250-41 at PA= -69° , covering the rest-frame wavelength range $4860 - 5080\text{\AA}$. The spectrum of the companion galaxy to the north east lies to the top of the image, and the slit intersects the western emission-line arc towards the bottom of the image. The emission lines visible on this image ($H\beta$, $[\text{OIII}]4959\text{\AA}$, $[\text{OIII}]5007\text{\AA}$) illustrate the complexity and extent of the EELR surrounding this source. The locations of our extracted apertures across the EELR are illustrated on the left hand side of this figure.

stantial portion of the EELR, the slit PA was chosen so as to also include flux from the possible companion galaxy 10.5 arcsec to the northeast.

Standard packages within the NOAO IRAF reduction software were used to reduce the raw data. Corrections were made for bias subtraction, and the data then flat-fielded using internal calibration lamp observations. The flat field images were made using the same instrumental set-up as the observations for each source. The 2-d spectra were corrected for geometric distortion, and then wavelength calibrated. The frames obtained in the 'o' and 'e' polarisation states were spatially aligned, combined, and cosmic rays removed. Polarisation results will be presented elsewhere (Tadhunter et al, in prep); in this paper we concentrate on the gas kinematics and ionization state. Flux calibration was carried out using observations of the spectrophotometric flux standard star LTT377, and the data were also corrected for atmospheric extinction. The data were corrected for Galactic extinction using $E(B - V)$ values for the Milky Way from the NASA Extragalactic Database (Schlegel et al 1998), and the empirical extinction function of Cardelli et al (1989).

Fig. 2 displays a limited section of the two-dimensional FORS1 spectrum (including the $H\beta$ and $[\text{OIII}]4959+5007\text{\AA}$ emission lines); the companion object continuum is clearly visible at the top of the image. It is also noteworthy that we detect faint very extended line emission between the two galaxies (see also Clark et al 1997).

2.3 VIMOS-IFU spectroscopic observations

Integral field unit (IFU) spectroscopic observations were carried out using the Visible Multiobject Spectrograph (VIMOS; Le Fèvre et al 2003, Scodreggio et al 2005), on 2004 October 19, 2004 November 19, 2005 June 7 and 2005 June 9, as part of the ESO observing programmes 074.B-0310(A) and 075.B-0820(A). VIMOS is mounted on the Nasmyth focus of the UT3 Melipal unit of the VLT. These data were obtained using the medium resolution (MR-orange) grism; using this configuration, the IFU consists of 1600 microlenses coupled to 0.67-arcsec diameter fibres, and covers a total sky area of $27 \times 27\text{ arcsec}^2$. The total useful wavelength range is $\sim 4500 - 9000\text{\AA}$, and the spectral resolution (as deter-

mined from unblended skylines) was $7 \pm 0.5 \text{ \AA}$. Two separate pointings were used, separated in RA and declination by ~ 2 arcsec and ~ 11 arcsec respectively. The total integration time was ~ 49000 s; full details of the observations and observing conditions are given in table 1.

Data reduction was carried out using the VIMOS Interactive Pipeline and Graphical Interface (VIPGI) software package (Scodreggio et al 2005, Zanichelli et al 2005). Our exact method includes some variations from the standard VIPGI procedures particularly during the sky-subtraction phase, and is detailed in full in Inskip et al (2007).

In this paper we concentrate on a limited region of the IFU data-cube, as illustrated by the box marked on Fig. 1.

2.4 SOFI Ks-band imaging

Infrared Ks-band imaging of PKS2250-41 was carried out on 2006 November 14 using the Son of ISAAC (SOFI; Moorwood, Cuby & Lidman 1998) instrument on the ESO 3.5-m New Technology Telescope (NTT). The instrument was used in the small field mode, which results in a plate scale of 0.144 arcsec per pixel. Fifty 1-min exposures were obtained, with each observation subject to a random offset within a 40 arcsec diameter box. The data were dark subtracted and corrected for SOFI's interquadrant row cross talk effect using an adapted version of the SOFI crosstalk.cl IRAF script. Flat-fielding of the data was carried out using the following process: all target frames were combined, median filtered and normalised to a mean pixel value of 1.0 to create a first-pass flat-field image, which was then applied to each frame. Bright objects on the flat-fielded images were then masked out, and the process repeated with the masked frames, allowing the data to be cleanly flat fielded without any contamination from stars or galaxies. The subsequent data reduction uses well-established techniques: the flat-fielded data were sky-subtracted and combined using the IRAF package DIMSUM, creating a final mosaiced image of approximately 180×180 arcsec². Flux calibration used observations of NICMOS Photometric Standard stars (Persson et al 1998), giving a photometric zero-point magnitude of $K_S = 22.347 \pm 0.010$. The data were corrected for galactic extinction using $E(B - V)$ values for the Milky Way from the NASA Extragalactic Database, and the parametrized galactic extinction law of Howarth (1983).

2.5 WFPC2 emission line imaging

In this paper, we will also make use of the previously published WFPC2 medium band and narrow band imaging of T05. The emission line imaging data were obtained using the HST WFPC2 linear ramp filters, with the target galaxy placed on the region of the chip sensitive to the observed-frame wavelength of either the [OIII]5007Å or [OII]3727Å emission lines. An intermediate-band continuum image was obtained using the F547M filter, to allow for continuum subtraction from the emission-line images, and examination of the continuum structures. We refer the reader to T05 for full details of the observations and the data reduction procedures used.

3 RESULTS

3.1 Results from the FORS1 spectrum

The 2-d profile of the major emission lines (Fig. 2, see also Fig. 5) is very asymmetric, reflecting the complex kinematics of the EELR. Relatively broad (up to $\sim 400 \text{ km s}^{-1}$) line emission is observed close to the host galaxy, with a clear linear velocity shift. The line emission to the northeast is blueshifted compared to that lying to the southwest of the host galaxy continuum centroid. Between the host galaxy and the companion, faint, narrower line emission is observed throughout the intervening space; this emission appears to have a uniform velocity shift at all spatial offsets. To the southwest of the host galaxy, we see the expected features of the emission line arc: line widths broadening to a maximum at the position of the peak line intensity.

We have extracted a number of one-dimensional spectra from this 2-d spectrum, in consecutive $1.6''$ apertures (Fig. 2). Fig. 3 presents the extracted 1-d spectrum across the nucleus of the host galaxy. The resulting emission line ratios (see appendix) have been used to investigate the ionization state of the gas, via the temperature sensitive [OIII]5007/[OIII]4363 vs. [OIII]5007/H β diagnostic diagram (Fig. 4). Where the [OIII]4363Å was too faint to be accurately measured, we use the 1-sigma upper limits for the line flux to determine a lower limit for the [OIII]5007/[OIII]4363 emission line ratio.

Close to the host galaxy centroid (extracted spectra S4, S5 and S6) the emission line ratios are consistent with AGN photoionization. The [OIII]4363Å could not be accurately measured for the emitting material lying further to the east (spectra S7, S8), but given the observed line widths, the line ratios for the extended narrow emission are most likely to be similar, reflecting AGN photoionization. To the west of the host galaxy, the spectra extracted across the emission line arc, i.e. the region of the EELR with the strongest impact from jet-cloud interactions (S1, S2 and S3) display a mixture of emission line ratios. S2 and S3, while only having lower limits for the [OIII]5007/[OIII]4363 line ratio, are more consistent with a shock plus precursor photoionization region ionization mechanism than with shock ionization alone. S1 lies beyond the radio lobe where jet-cloud interactions are not yet likely to have affected the gas strongly; comparison with S2 and S3 reflects the impact that such interactions have on the observed line ratios. Overall, these results are fully consistent with those determined from the spectroscopic studies of VM99 and Clark et al (1997).

We will now consider the central regions of the EELR in more detail.

3.1.1 The velocity curve of the inner 2''

The line-emitting gas close to the host galaxy has a number of interesting features. In Fig. 5, we display a continuum-subtracted image of the [OIII]5007Å emission line from the two-dimensional FORS1 spectrum. Also displayed are the emission line velocity shifts and FWHM, evaluated on a pixel-by-pixel basis, with the spatial zero taken at the position of the continuum centroid. The FWHM (after correcting for instrumental broadening) varies in the range $\sim 150 - 410 \text{ km s}^{-1}$, with a maximum at the position of the

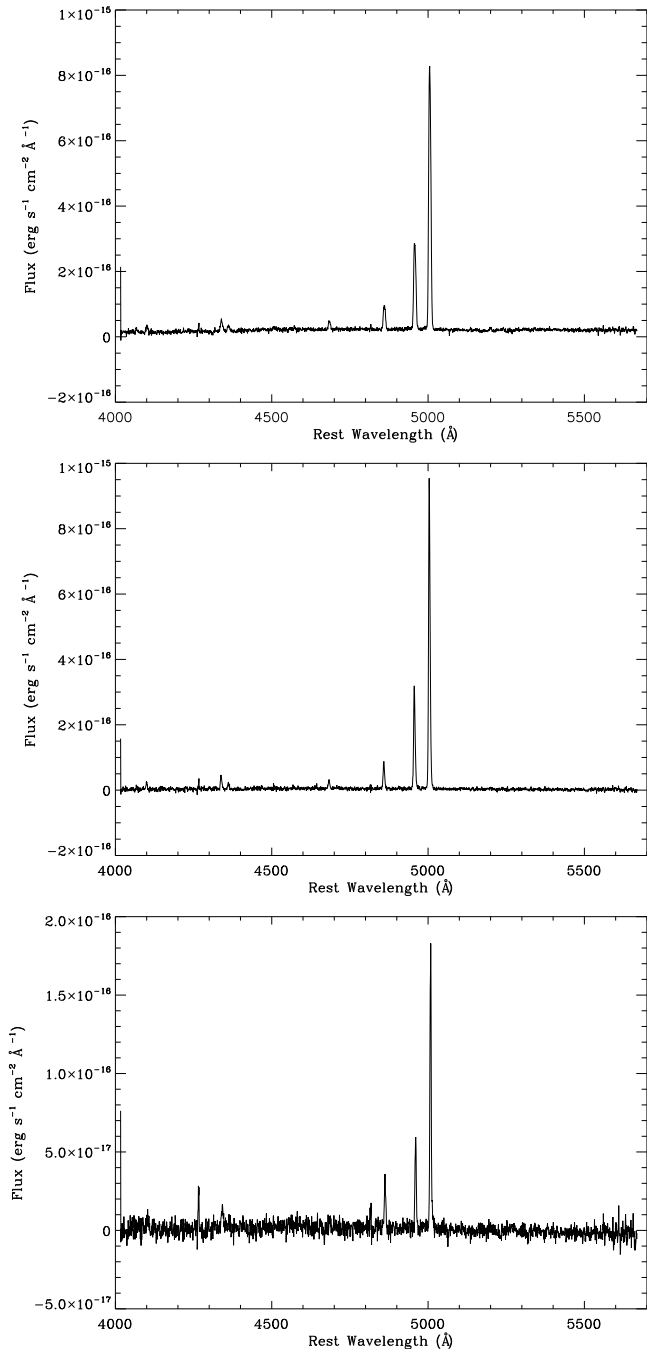


Figure 3. Examples of the FORS1 spectra of PKS2250-41, extracted from three different $1.6''$ apertures: (a - top) centred on the continuum centroid, (b - centre) the narrower photoionized filamentary emission northeast of the nucleus, and (c - bottom) material in the shocked emission-line arc.

continuum centroid (possibly due to unresolved rotation in the central regions). The line emission is asymmetric at some spatial offsets, where the line profile is better reproduced by multiple Gaussian components. While the line broadening and asymmetries might be expected to distort the velocity profile, the fact that it remains remarkably smooth and does not display sharp changes at the position of maximum line

broadening suggests that the overall kinematic pattern of the gas is not severely distorted.

At this point, it is interesting to examine in detail the high surface brightness emission line features present in the HST imaging observations of T05. Figure 6 displays a continuum-subtracted $[\text{OIII}]5007\text{\AA}$ emission line image of the EELR, with the contrast levels adjusted to best display the morphology of the high surface brightness features in the central $3 - 4\text{arcsec}$. Line emitting material extends out from the galaxy nucleus along the same position angle as the spectroscopic slit, i.e. in the direction of the companion galaxy; the eastern emission is brighter and has a less regular shape. Fainter line emission surrounds these structures, filling the spectroscopic slit.

It is possible that the difference between the seeing ($\sim 0.56''$) and the slit width ($\sim 1.3''$) could have introduced an erroneous instrumental profile: in the case of an unresolved emission feature which does not fill the slit completely, the instrumental profile would be 2.54\AA rather than the $5.9 \pm 0.2\text{\AA}$ measured from the sky and arc lines. Although the emission line imaging observations confirm that line emission does indeed fill the FORS1 slit (Fig. 6), the brightest features clearly occupy a more confined region within the bounds of the slit, and are therefore a potential problem. While this could potentially lead to artificial velocity shifts, the close similarity between the kinematics derived from the FORS1 observations and the VIMOS observations suggest that there is no problem in this respect.

There are several possible interpretations for the observed gas kinematics. On the basis of the FORS1 spectrum alone, the gas kinematics are consistent with a $\sim 15\text{kpc}$ diameter rotating disk, and an implied lower limit to the dynamical mass of $M\text{sin}i^{-1} \sim 2 \times 10^{10}M_{\odot}$ within a $1\text{arcsec}/4.55\text{kpc}$ radius. Although this is a lower limit, the morphology of the EELR (Fig. 6) would suggest a close to edge-on orientation for any disk system present. Alternatively, the observed velocities could be caused by other means, with the observed line emission originating primarily from the edges of an ionization cone. Close inspection of Fig. 6 suggests that there is a dearth of emission *directly* along the east-west aligned radio source axis, suggesting a hollowed-out region between the brightest emission extending NE-SW and the fainter emission extending SE-NW. This is similar to the conic features observed in Cygnus A (Taylor et al 2003; Tadhunter et al 1999; Jackson et al 1998). We note further that that the observed velocity amplitude displayed in Fig. 5 is much less than that observed in other galaxies with gas undergoing regular rotation (e.g. Tadhunter et al 1989, Baum et al 1990). Other alternative explanations which should be considered are inflows or outflows imperfectly aligned with the radio source axis (see Fig. 6).

3.2 IFU Spectroscopy

As the EELR of PKS2250-41 are known to be so complex, integral field spectroscopy is a particularly effective means of disentangling the varied kinematic components. In this section, we will discuss the different properties of the EELR in turn, focusing on the EELR morphology, kinematics and ionization state. In order to best illustrate the different features of the EELR, we present our IFU data in several different ways.

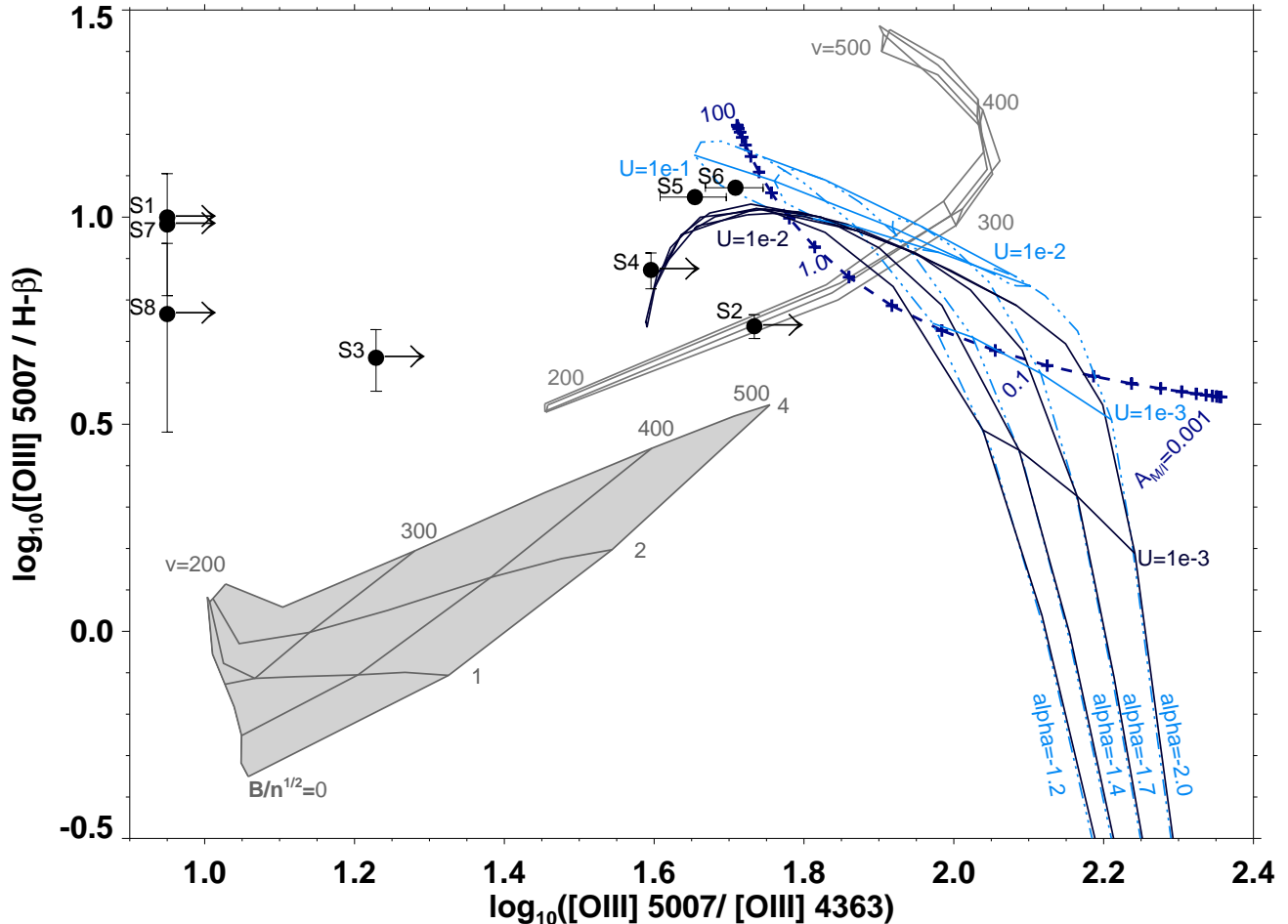


Figure 4. Emission line diagnostic plot for the PA-69 FORS1 spectrum of PKS2250-41, using the line ratios $[\text{OIII}]5007/[\text{OIII}]4363$ and $[\text{OIII}]5007/H\beta$. Data points represent spectra extracted in $1.6''$ steps along the slit (see Table 2 and Fig. 2 for details). Lower limits are given for the $[\text{OIII}]5007/[\text{OIII}]4363$ line ratio in the cases where the $[\text{OIII}]4363\text{\AA}$ emission line is undetected. The model tracks include: (1) shock ionization (Dopita & Sutherland 1996), with and without a precursor photoionization region (unshaded and shaded respectively), (2) the matter-bounded photoionization track (dashed dark blue track, Binette, Wilson & Storchi-Bergmann 1996), and (3) simple AGN photoionization tracks (light blue tracks), including the effects of dust (solid black tracks; Groves, Dopita & Sutherland 2004a,b). The photoionization models are for $n=1000\text{ cm}^{-3}$, solar metallicity and various values of the ionization index α (from $1.2 < \alpha < 2.0$).

The figures in this section (7, 8 and 9) concentrate on our chosen region of the IFU data cube (illustrated in Fig. 1b), which covers the majority of the radio cocoon. In order to study the EELR properties in greater detail, we have developed IDL routines to model the line emission on a fibre-by-fibre basis. For each fibre spectrum, we locate a selected emission line and fit it with one or more Gaussian components plus a continuum, extracting the resulting modelled emission-line flux, FWHM and velocity offset relative to the systemic redshift of PKS2250-41. Fig. 7 displays the variation in the fluxes of the $[\text{OIII}]5007\text{\AA}$ and $[\text{OII}]3727\text{\AA}$ emission lines across the EELR, and also the changing $[\text{OIII}]5007\text{\AA}/[\text{OII}]3727\text{\AA}$ line ratio for the same region. Fig. 8 displays the kinematic properties of the modelled $[\text{OIII}]5007\text{\AA}$ and $[\text{OII}]3727\text{\AA}$ emission lines.

3.2.1 The EELR morphology

The EELR surrounding PKS2250-41 displays a number of different features. The brightest $[\text{OII}]$ line emission is lo-

ated close to the host galaxy and is approximately co-spatial with the continuum centroid. This is in good agreement with previous spectroscopic studies of this source (VM99, Clark et al 1997). However, the line emission is noticeably elongated, with the long axis orientated along approximately the same angle as the FORS1 slit and the filamentary line emission displayed in Fig. 6. Although faint line emission is observed along this PA for a considerable distance in our FORS1 spectrum, the IFU data only detect this emission relatively close to the host galaxy. Faint emission is observed in the IFU data cube to the south east of the host galaxy, coincident with some of the features observed in the ground-based emission line imaging observations of Clark et al (1997). The powerful emission-line arc is also clearly detected in our IFU data. However, we also observe fainter emission filling the region between the host galaxy and the emission-line arc.

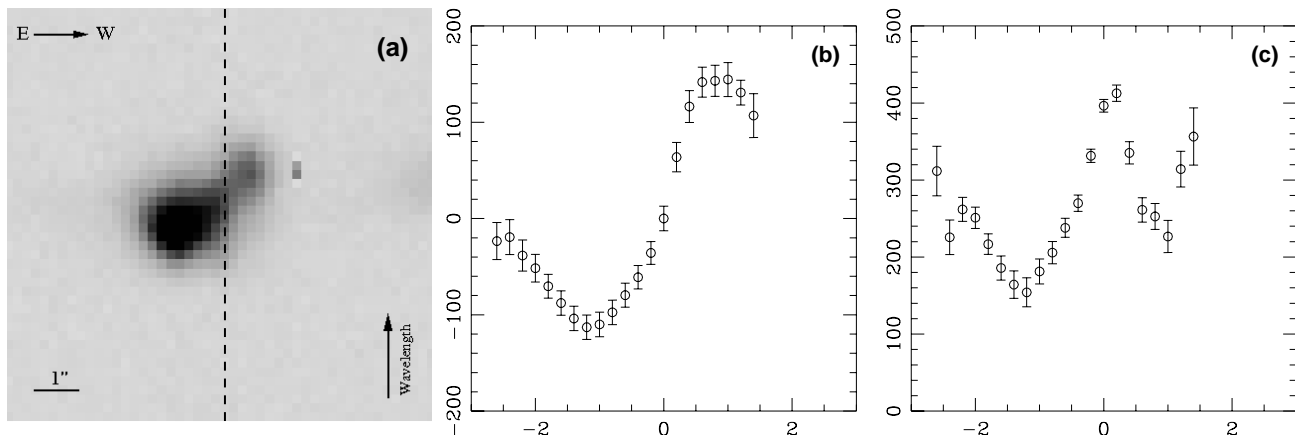


Figure 5. Left: Inner 4'' (~ 18 kpc) region of the FORS1 spectrum (PA 69°), illustrating the continuum-subtracted [OIII]5007Å emission line (the continuum centroid location is indicated by the dashed line). Centre: [OIII]5007Å emission line velocity shift (km s^{-1}) as a function of offset (east to the left, west to the right, measured in arcsec) from the continuum centroid. Right: [OIII]5007Å emission line FWHM (km s^{-1}) as a function of offset (arcsec) from the continuum centroid. All velocities are in the rest-frame of the galaxy. As a reminder, 1 arcsec is equivalent to 4.55kpc in our assumed cosmology.

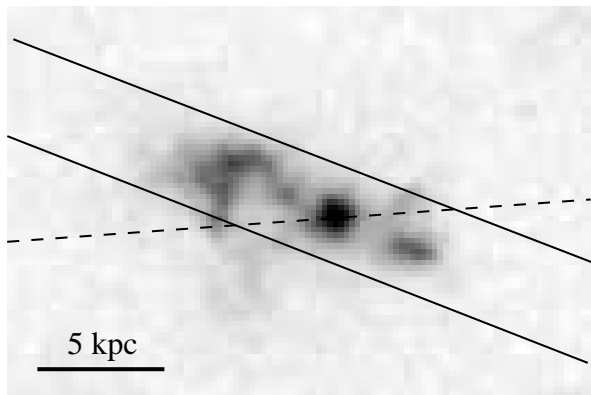


Figure 6. Drizzled WFPC2 [OIII]5007Å emission-line image of the central regions of the EELR surrounding PKS2250-41, illustrating the strongest line emission. The position of the FORS1 slit is marked by the angled lines. The radio source axis is aligned approximately east-west, and is marked by the dashed line. In this figure, north is to the top and east to the left.

3.2.2 Ionization of the emission line gas.

As Fig. 7c demonstrates, the ionization state of the gas varies quite strongly across the EELR. The ratio of [OIII]5007Å/[OII]3727Å is at its highest close to the host galaxy nucleus, consistent with AGN photoionization dominating in this region. The [OIII]5007Å/[OII]3727Å line ratio is much lower towards the western emission line arc, reaching a minimum level at the position of the radio source hotspot, where jet-induced shocks are likely to dominate. Westwards of the most intense emission in the arc the oxygen line ratio rises once again. It is also noteworthy that a lower ionization state is observed *along* the radio source axis, with (relatively) stronger [OIII] emission to either side. Again, these results are consistent with those of VM99 and Clark et al (1997).

3.2.3 EELR kinematics

One feature which is immediately obvious from our IFU data is the velocity shift across the western emission line arc; as Fig. 8 illustrates, the material to the north of the arc is clearly blueshifted with respect to the emitting material in the southern portions of the arc, and the pixel to pixel variation is generally quite smooth. This is consistent with the data obtained from the current and previous long-slit spectroscopic studies, but the observed velocity shift is far more readily apparent in the IFU data. The north-south velocity shift across the EELR is in the range $100\text{-}300\text{km s}^{-1}$. Such a general north-south divide between redshifted and blueshifted material is suggestive of bulk rotation, though as noted in section 3.1.1, the observed velocities are somewhat on the low side.

In terms of the widths and profiles of the emission lines, the broadest and most complex emission is observed along the radio source axis, between the host galaxy centroid and the radio source hotspot. The emitting material towards the outer edge of the western arc displays relatively narrow emission lines, as does the emission extending into the eastern radio lobe.

In order to analyse our IFU spectra at a higher signal-to-noise level and address the issue of superposed velocity structures, we have extracted and combined the spectra of fibres covering specific emission regions, and those which display similar kinematic properties. The resulting regions, labelled numerically from I to XII, are displayed in Fig. 9. We have re-analysed the [OIII]5007Å line widths and velocity shifts, fitting up to three Gaussians to the combined emission line data. The results of our kinematic analysis are consistent between different lines, and with the single-fibre data displayed in Fig. 8; we tabulate the results for [OIII]4959,5007 in Table 2. These results are also in good agreement with those of the current FORS1 spectroscopy and the earlier spectroscopy of Clark et al (1997), Tadhunter et al (1994) and VM99.

The narrowest emission line components are observed

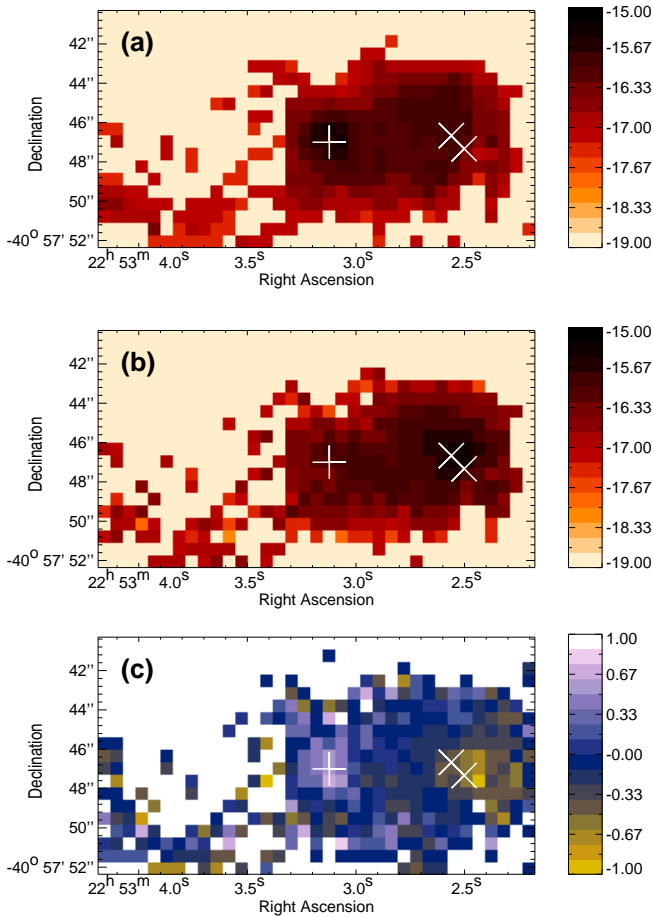


Figure 7. From top: (a) extracted [OIII]5007Å line flux, (b) extracted [OII]37277Å line flux, and (c) [OIII]5007Å/[OII]37277Å emission line ratio derived from the VIMOS data cube. These results are based on single gaussian fits. The position of the host galaxy centroid is marked in all frames by '+', and the position of the two western-lobe radio hotspots by 'x'. For comparison with the radio and continuum structures, we refer the reader back to Fig. 1b. The grey-scale bars for the flux images are logarithmic, in units of $\text{ergs}^{-1}\text{cm}^{-2}$. The scale bar for frame (c) is logarithmic and dimensionless. North is to the top and east to the left, the pixel scale is $0.67''/\text{pixel}$ (giving a total field of view of $\sim 23.5 \times 13$ square arcsec, or $\sim 110 \times 60\text{kpc}^2$ at a redshift of $z = 0.308$).

in the eastern radio lobe; the line emission from regions I, II and V has instrumentally corrected component line widths of the order of $130\text{--}200\text{km s}^{-1}$. However, even at these low FWHM values the velocity shift between the northern and southern parts of the EELR is clear. Similarly quiescent material with relatively narrow instrumentally corrected line widths ($100\text{--}200\text{km s}^{-1}$) is also observed in the western radio lobe, between the host galaxy and the emission line arc (regions VII, IX, X, XI).

The next notable feature is line emission with FWHM roughly of the order of 400km s^{-1} , which is observed in several consecutive regions: III, IV, VI, VIII. Interestingly, the emission from these regions lies along the same PA as the bright emission line filament illustrated in Fig. 6 and the FORS1 slit; our measured FWHM and velocity shifts for these regions are also consistent with those displayed in Fig. 5. However, as the spectra for regions III and VIII have

Table 2. Kinematics of the multi-fibre regions illustrated in Fig. 9. Velocity shifts are relative to the typical value of $z = 0.3074$.

Region	FWHM (km s^{-1})	Velocity Shift (km s^{-1})	Reduced χ^2
I - single	197 ± 32	278 ± 35	1.54
II - single	144 ± 32	-136 ± 35	1.60
III - single	436 ± 14	-69 ± 35	2.52
IV - single	438 ± 2	-10 ± 34	5.93
IV - double	381 ± 3	-8 ± 34	5.52
	700 ± 16	-21 ± 35	
V - single	335 ± 8	162 ± 34	3.59
V - double	138 ± 14	173 ± 34	2.26
	819 ± 44	92 ± 40	
VI - single	479 ± 11	130 ± 34	1.60
VI - double	409 ± 12	155 ± 34	1.55
	668 ± 55	21 ± 42	
VII - single	442 ± 6	-55 ± 34	2.58
VII - double	169 ± 13	-37 ± 34	1.60
	620 ± 12	-74 ± 34	
VIII - single	410 ± 59	295 ± 41	2.33
IX - single	204 ± 5	57 ± 34	2.17
IX - double	172 ± 5	59 ± 34	1.95
	819 ± 130	-85 ± 69	
X - single	319 ± 4	22 ± 34	5.86
X - double	174 ± 6	33 ± 34	1.07
	940 ± 32	-93 ± 37	
X - triple	122 ± 9	33 ± 34	0.97
	1037 ± 184	-619 ± 94	
	699 ± 11	-4 ± 34	
XI - single	327 ± 6	129 ± 34	2.66
XI - double	215 ± 7	129 ± 34	1.72
	819 ± 45	120 ± 40	
XII - single	274 ± 12	122 ± 34	2.17

lower signal-to-noise levels than some of the other regions, we cannot conclusively rule out a combination of broader and narrower components; such degeneracies are a common issue in the analysis of emission line profiles. This may also be the case for region XII, where the measured FWHM of 274km s^{-1} could perhaps be better explained by broader emission associated with the arc lying adjacent to more quiescent material. The emission from region XII lies beyond the main emission line arc and the western radio lobe and is at lower signal to noise than the inner regions of the EELR. Although a weak velocity gradient is observed across this region (Fig. 8b), we cannot conclusively confirm that the same apparent pattern of rotation holds true in this region as well as in the inner EELR.

There is also some level of consistency between the regions lying directly along the radio source axis (IV, VI, VII, IX, X, XI), all of which feature a kinematic component with FWHM between $\sim 600 - 820\text{km s}^{-1}$. But once again, even these higher-velocity features are subject to the same north-south gradient in relative velocity. This suggests that all of the different velocity components present in the line-emitting gas are subject to the same underlying pattern of rotation.

Finally, the highest gas velocities are observed (as expected) in close proximity to the radio source hotspot in the western radio lobe, where we detect components with line widths of over 1000km s^{-1} .

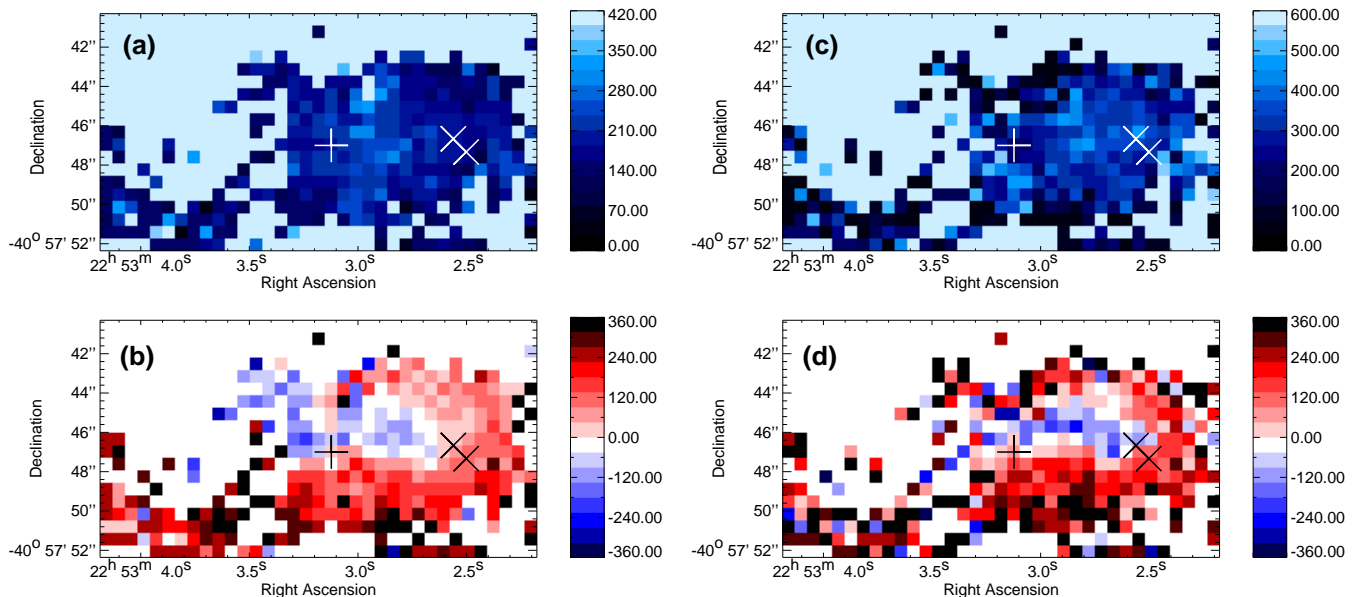


Figure 8. IFU emission line kinematics. (a - top left) $[\text{OIII}]5007\text{\AA}$ FWHM line width (corrected for instrumental broadening). (b - lower left) velocity shift of $[\text{OIII}]5007\text{\AA}$ relative to $z = 0.3074$. (c - top right) $[\text{OII}]3727\text{\AA}$ FWHM line width (corrected for instrumental broadening). (d - lower right) velocity shift of $[\text{OII}]3727\text{\AA}$ relative to $z = 0.3074$. These results are based on single gaussian fits. The position of the host galaxy centroid is marked in all frames by ‘+’, and the position of the two western-lobe radio hotspots by ‘x’. In these plots, we have masked the fibres with an $[\text{OIII}]5007\text{\AA}$ emission line flux below $1 \times 10^{-18} \text{ergs}^{-1} \text{cm}^{-2}$. The colour bars denote velocities in units of kms^{-1} . North is to the top and east to the left, the pixel scale is $0.67''/\text{pixel}$ (giving a total field of view of $\sim 23.5 \times 13$ square arcsec, or $\sim 110 \times 60 \text{kpc}^2$ at a redshift of $z = 0.3074$).

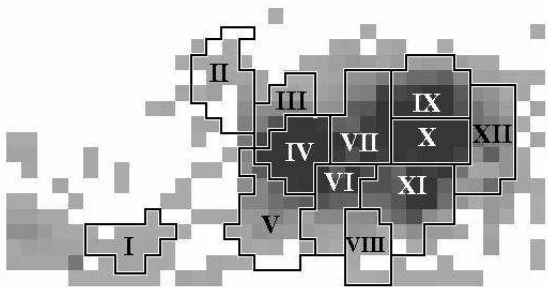


Figure 9. $[\text{OIII}]5007\text{\AA}$ IFU flux image illustrating the twelve multi-fibre regions extracted as part of our higher signal-to-noise analysis of the EELR. Regions have been selected according to similar kinematic properties of adjacent fibres. North is to the top and east to the left, the pixel scale is $0.67''/\text{pixel}$ (giving a total field of view of $\sim 23.5 \times 13$ square arcsec, or $\sim 110 \times 60 \text{kpc}^2$ at a redshift of $z = 0.308$). The galaxy nucleus lies within region IV, while the bright emission line arc to the west of the galaxy is covered by regions IX, X and XI.

3.3 The host galaxy

Figure 1b displays our recent K_S -band imaging observations of PKS2250-41. The radio galaxy itself is an elliptical with a total K_S -band magnitude (galactic extinction corrected and evaluated within a 10 arcsecond/45.5 kpc diameter aperture) of 15.56 ± 0.05 , placing it towards the fainter range of host galaxy magnitudes in the radio source K-z relation (e.g. Inskip et al 2002a; Inskip et al 2008 *in prep*). We have modelled the host galaxy morphology within a

$32 \times 32 \text{arcsec}^2$ region using the methods detailed in Inskip et al. (2005), which can be briefly summarised as follows. The point spread function (PSF) for the SOFI field can be accurately determined from unsaturated stars towards the centre of the mosaic field; their 2-d profile is extracted, normalised to unit flux, and used to generate an average PSF profile. Once a good PSF had been obtained, de Vaucouleurs profile galaxy models were convolved with the PSF and fitted to the surface profile of the galaxy, using available least squares minimisation IDL routines¹. The free parameters for this modelling are the galaxy flux, centroid, effective radius, and fractional nuclear point source contribution. Galaxy ellipticity was also allowed to vary, but in the case of this object did not lead to significant variation in the preferred effective radius, nuclear point source contribution, or distribution of residual flux.

The modelled data and model-subtracted residuals are displayed in Fig. 10, together with a plot of the variation in reduced χ^2 over the parameter space considered. The resulting best-fit parameters give an effective radius of $r_{\text{eff}} = 1.42 \pm 0.77 \text{arcsec}$ (equivalent to $6.47 \pm 3.51 \text{kpc}$ in our assumed cosmological model), and an unresolved nuclear point source contribution of $21.2 \pm 4.9\%$; the residuals are comparable to the background noise. After subtraction of the point source component, the remaining near-IR flux is comparable to that of a $\sim 1.4L_*$ galaxy at a redshift of ~ 0.31 (Willott et al 2003).

Assuming that the point source component is non-

¹ MP2DFUNFIT.PRO, part of Craig Markwardt’s MPFIT non-linear least squares curve fitting package available via <http://astrog.physics.wisc.edu/~craigm/idl/fitting.html>.

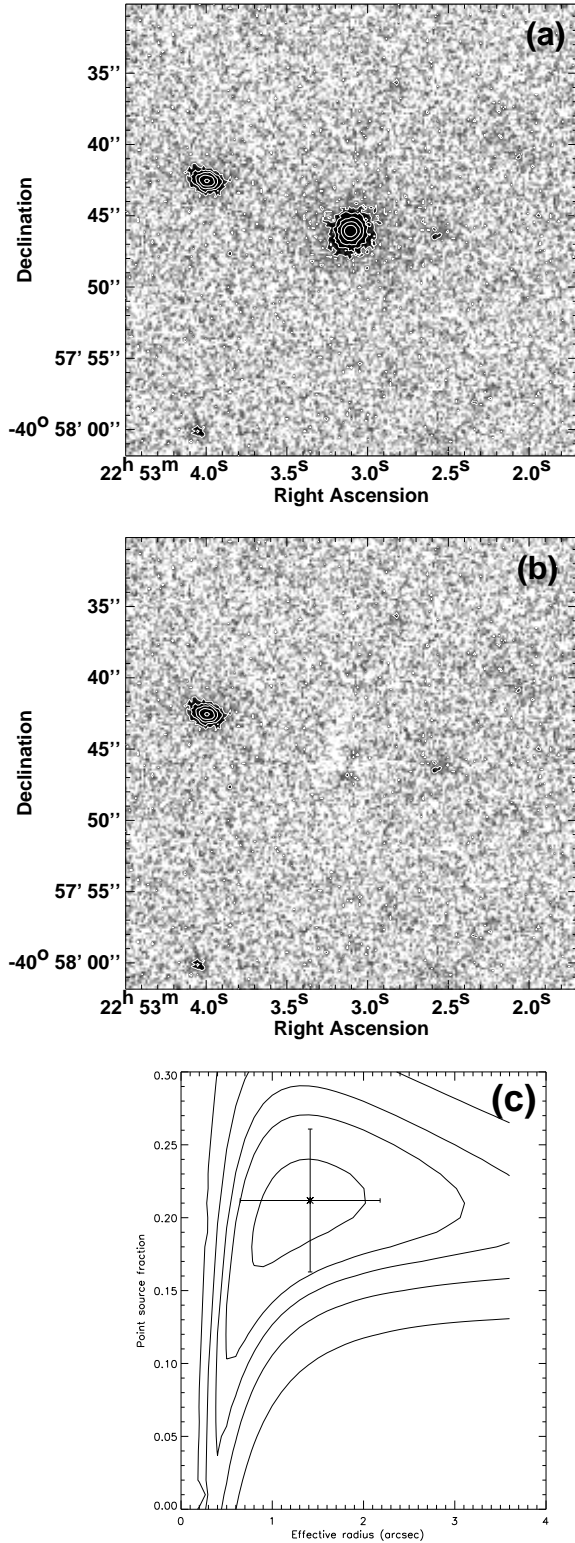


Figure 10. Host galaxy morphology fits for PKS2250-41. The K -band galaxy image is presented in frame (a), with the residuals after best-fit model galaxy subtraction displayed in frame (b). Frame (c) illustrates the 1, 2, 3, 5 and 10- σ contours for the reduced χ^2 , plus the best-fit values and associated error bars for the point source contribution and effective radius.

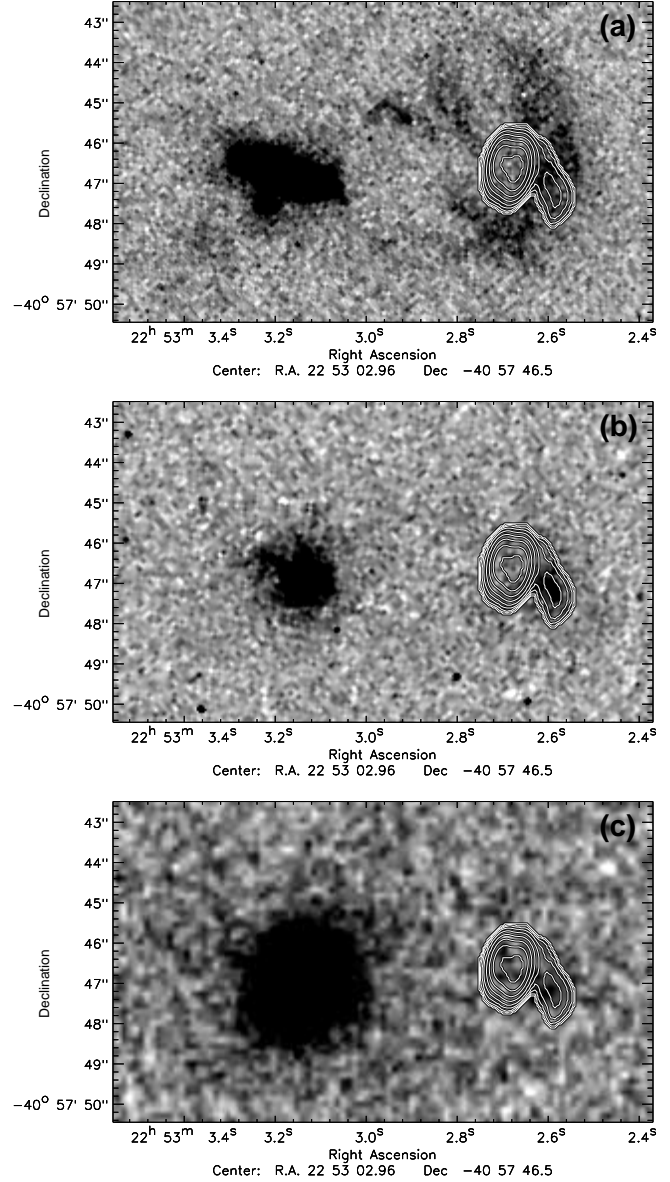


Figure 11. (a - top) WFPC2 [OIII]5007Å emission line image of PKS2250-41 overlaid with 15GHz VLA radio contours. (b - centre) WFPC2 F547M continuum image of PKS2250-41 overlaid with 15GHz VLA radio contours. (c - bottom) SOFI Ks-band image of PKS2250-41 overlaid with 15GHz VLA radio contours. Both the optical and infrared images display flux at the position of peak emission line intensity in the western arc, which is also coincident with the secondary hotspot within the western radio lobe. The WFPC2 and radio data are taken from T05.

stellar in nature, and that the bulk old stellar population of the galaxy formed at high redshift (i.e. $z = 5 - 20$), the galaxy flux can be modelled by a 9.5Gyr old stellar population. We have convolved a 9.5Gyr GISSSEL spectral synthesis (Bruzual & Charlot 2003) template spectrum with the K_S -band filter profile. Comparing the resulting flux with that measured for PKS2250-41 (after subtraction of the point source contribution measured via our modelling) suggests a total stellar mass for the galaxy of $2.1 \pm 0.5 \times 10^{11} M_{\odot}$.

We have also carried out aperture photometry of the

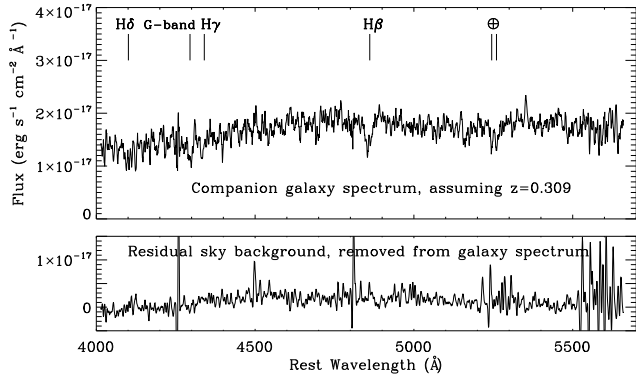


Figure 12. Smoothed FORS1 spectrum of the companion object lying ~ 10.5 arcsec to the north west of PKS2250-41, extracted from a $1''$ aperture centred on the continuum centroid. Absorption line features consistent with a redshift of $z = 0.309$ are labelled. We also plot the residual sky background.

host galaxy using the F547M WFPC2 data of T05, obtaining a host galaxy magnitude in this filter of 20.54 ± 0.12 . Comparison of the relative flux densities observed in each of the two continuum filters (F547M and K_S) confirms that they are consistent with the spectral energy distribution expected for a 9.5Gyr old stellar population.

It is interesting to note that the filamentary line emission displayed in Fig. 6 is matched by an extension in the optical continuum observed from this galaxy along the same position angle (Fig. 11). The extension to the host galaxy is clearly visible in the optical, and it is also noteworthy that the lowest surface brightness IR emission is somewhat disturbed in this region of the galaxy, perhaps reflecting a distortion in the underlying galaxy structure.

3.4 Companion objects

Figure 12 displays the FORS1 spectrum for the companion galaxy to the north east, extracted within a $1''$ aperture. The strongest feature in the spectrum is an absorption line consistent with $H\beta$ at a redshift of $z = 0.309$. The continuum shape is also generally consistent with a galaxy at the assumed redshift, and we also see a noisy absorption features at wavelengths appropriate to the G-band, $H\gamma$ and $H\delta$.

Using the WFPC2 continuum data of T05 and the IR data presented in this paper, we have carried out aperture photometry of this source. In the optical, this companion galaxy has a magnitude of 20.57 ± 0.12 , slightly fainter than the radio source host galaxy. In the IR, the observed K_S -band magnitude is 16.48 ± 0.08 . The relative flux densities of the observed-frame optical and infrared emission from this galaxy are consistent with a single old stellar population (OSP) aged between 2-4Gyr. However, given the presence of Balmer absorption features in this galaxy a composite stellar population including both old and young stars is likely to provide a more accurate description of this galaxy.

Past studies of PKS2250-41 have suggested that the prominent emission line arc to the west of the host galaxy originates from a direct collision between the radio source jet and a companion galaxy (Clark et al 1997, VM99). Figure 11 displays the infrared and optical continuum and the [OIII] emission line imaging data for PKS2250-41 overlaid with ra-

dio contours (all data except infrared from T05). Continuum emission is detected in both the K_S and F547M filters within the arc, coincident with the secondary radio hotspot. We have determined the flux density of this feature in both filters; the resulting ratio of F547M/ K_S emission is $24.3 \pm 58\%$. This value is consistent with unreddened stellar populations aged between either 0.006-0.009Gyr or 0.05-0.1Gyr, or alternatively reddened YSPs of even younger ages.

4 DISCUSSION

4.1 The evidence for jet-induced star formation.

For many years now it has been known that radio source jets have the potential to substantially affect the ambient interstellar/intergalactic medium. Separating the influence of the jet from other forms of the alignment effect (Chambers, Miley & van Breugel 1987, McCarthy et al 1987), i.e. scattered AGN emission or line and nebular continuum emission associated with AGN-ionized clouds, is not always straightforward (e.g. Tadhunter et al 2002; Inskip et al 2005) but in many cases there is clear-cut evidence for so-called ‘jet-cloud interactions’. This may take the form of shocks associated with interactions between the radio jet and cool gas clouds in the ISM/IGM, or alternatively, jet-induced star formation.

Jet-induced star formation was first proposed in order to explain the observations of such sources as Centaurus A (Blanco et al 1975; Graham & Price 1981; Brodie, Königl & Bowyer 1983; Sutherland, Bicknell & Dopita 1993; Schiminovich et al 1994; Oosterloo & Morganti 2005) and Minkowski’s Object (van Breugel et al 1985; Croft et al 2006). Current theoretical models (e.g. Fragile et al 2004; Mellema, Kurk & Röttgering 2002, and references therein) suggest that radio source shocks propagating through the clumpy ISM/IGM trigger the collapse and/or fragmentation of overdense regions, which may then subsequently form stars. Good evidence for jet-induced star formation has also been observed in the case of the radio sources 4C 41.17 (Dey et al 1997; Bicknell et al 2000), 3C34 (Best, Longair & Röttgering 1997) and 3C48 (Stockton et al 2007), but on the whole, while evidence for shocks associated with the radio source is relatively common, jet-induced star formation is far less frequently observed. PKS2250-41 is an archetypal example of a galaxy displaying jet-cloud interactions, with clear-cut evidence for shocks associated with the expanding radio source; specifically, via the observed variation in ionization state and gas kinematics in the vicinity of the western radio lobe hotspots (Clark et al 1997; VM99; T05). However, the origin of the emitting material and the case for jet-induced star formation is less absolute, and we therefore reconsider the issue here.

The primary evidence is the continuum emission which, in addition to the well-studied line emission, is also observed within the western radio lobe. The continuum emission is approximately co-spatial with the secondary radio source hotspot (Fig. 1), has low polarization (Shaw et al 1995) and only a limited contribution of nebular continuum emission (Dickson et al 1995). Clark et al (1997) suggested that the residual continuum emission could originate from a late-type spiral or irregular galaxy, with which the radio jet has collided; radio source shocks driven through the gas clouds as-

sociated with such an object can also account for the impressive scale and luminosity of the observed emission line arc, and possibly also the shortness of the western lobe relative to the eastern lobe.

Our infrared observations of PKS2250-41 add further weight to this scenario; the faint detection in the western lobe lies at an identical position to the optical continuum position. However, the inferred spectral shape implies that a *very* young stellar population is dominating the optical emission, suggesting that the proximity of the radio source may very well have triggered recent star formation within this object.

4.2 Interactions in a group environment.

Our spectroscopic observations of the companion galaxy to the north east confirm that it lies at an almost identical redshift to PKS2250-41 ($z = 0.3090 \pm 0.0005$ cf. $z = 0.3074$). The companion galaxy colours and the presence of Balmer absorption features in its spectra suggest that it is currently forming stars. A further interesting feature is that the position angle of the major axis of this galaxy is closely aligned with the line emission extending outwards from the radio galaxy (see Fig. 6). It therefore seems highly plausible that both galaxies form part of an interacting group, a similar environment to that of the radio source PKS1932-46 (Inskip et al 2007).

4.2.1 *Up close and personal: a recent interaction?*

In their paper on the emission line and continuum imaging of PKS2250-41, Tilak et al (2005) highlighted the presence of a continuum emission spur extending from the host galaxy, aligned towards the neighbouring companion galaxy to the north east (see also Fig. 11b), and coincident with the brightest line emission (see also Fig. 6). Additionally, the position angles of both spur and companion differ by no more than 6° , while the filamentary line emission surrounding the spur is even better aligned with the companion galaxy.

The presence of this filamentary feature has profound implications for our understanding of how this particular radio source was triggered. At present, there are several different mechanisms by which the fuelling of the AGN may occur. Fuel may be supplied by the infall of cooling gas (Bremer, Fabian & Crawford 1997), though this is most likely to cause a renewal of the AGN activity in a galaxy rather than being related to the earliest triggering of the source (Nipoti and Binney 2005). Alternatively, a merger between two galaxies, one of which is gas-rich, can lead to fuelling of the AGN (e.g. Heckman et al 1986; Barnes & Hernquist 1996; Mihos & Hernquist 1996); the ensuing AGN activity may occur contiguously (e.g. di Matteo, Springel & Hernquist 2005) or after a substantial delay (e.g. Sanders et al 1988), and in many cases is associated with the presence of young- to intermediate-aged stellar populations (e.g. Tadhunter et al 2005). In the case of PKS2250-41, we may indeed be observing direct physical evidence of the specific event which led to the triggering of the radio source activity within the galaxy.

While our data suggest that the observed filamentary feature could be consistent with a large-scale rotating structure (e.g. Fig. 13a), there is an order of magnitude discrepancy between the stellar mass estimated from the K-band

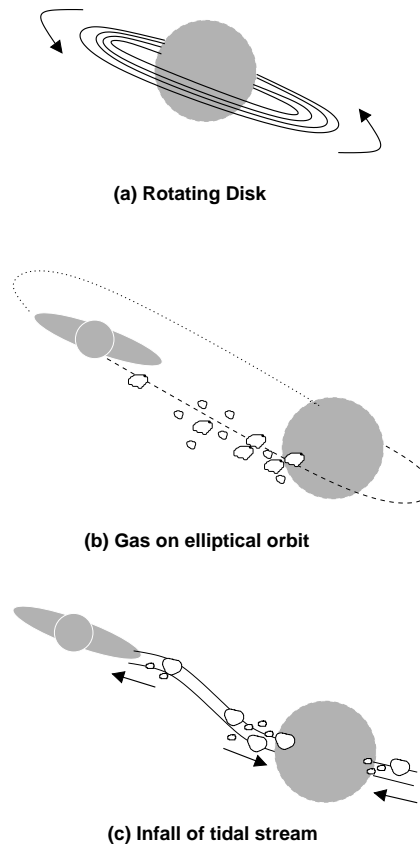


Figure 13. Three sketches illustrating the different interpretations of the origin of the emission line and continuum spur (see Fig. 6 and Fig. 11a,b), as described in full in section 4.2.1. Frame (a) illustrates the case of gas in a rotating disk structure orbiting the host galaxy, frame (b) gas strewn along the elliptical orbit of the companion galaxy to the northeast, and frame (c) the infall of material along the tidal stream between the two galaxies.

magnitude and the mass estimated from the ‘rotation curve’ of the emission lines. If the observed feature is indeed a rotating disk, the morphology of the emission would require it to be nearly edge-on. Given this fact and the mass discrepancy, we thus rule out a fully sampled rotating disk in dynamical equilibrium with the host potential being the source of the highest surface brightness aligned features. However, it is possible that we might be observing a disk feature which is not fully sampled, and may only be observing the part of it which lies within the ionization cone of the quasar.

The observations might instead be better explained by gas strewn along the elliptical orbit of the companion, which is seen almost edge-on (see Fig. 13b). In this case, the gas observed close to the nucleus of PKS2250-41 could be moving almost perpendicularly to the line of sight, particularly if this gas doesn’t sample the perigee of the companion’s orbit. The higher surface brightness of the emission closer to the nucleus would be due to the gas being lit up by the quasar; the offset of the emission from the radio axis is naturally explained in this scenario. The exact form of the velocity curve would depend on the distribution of gas around the orbit, and could easily account for the observations.

Another option is a tidal streamer pulled off from the

disk of the radio source precursor object by the companion galaxy (see, e.g., the numerical simulations of di Matteo et al (2005)). At some stages following the first pass of the two merging galaxies the gas will stream back (almost radially) towards the nuclei of the galaxies (see Fig. 13c). In this case, the velocity curve could reflect the streaming infall motions on either side of the nucleus. Such infalling material could be responsible for triggering the AGN/jet activity within PKS2250-41.

4.2.2 The triggering of the activity

Spitzer MIPS photometry of a complete sample of 2Jy sources (Tadhunter et al 2007) has been used to address the issue of the dominant dust heating mechanism in AGN. The [OIII]5007Å emission line luminosity (which can be used as a tracer of AGN power, e.g. Rawlings & Saunders 1991; Tadhunter et al 1998; Simpson 1998) is strongly correlated with the mid-IR emission (see Fig. 1 in Tadhunter et al 2007), indicating that AGN illumination is the principal dust-heating mechanism. The mid- to far-IR fluxes of PKS2250-41 (22mJy and 11.6 mJy at 70μm and 24μm respectively) imply an overall far-infrared luminosity of $L_{IR} \sim 2 \times 10^{11} L_{\odot}$ (Sanders & Mirabel 1996). Although this is consistent with a LIRG-class source, this source falls firmly on the correlation between mid- to far-IR emission and the [OIII]5007Å emission line luminosity, suggesting that in the case of this source the mid- to far-IR luminosity is derived from AGN rather than starburst illumination. Further to this, the mid- to far-IR emission is well centered on the centroid of the radio source host galaxy, with no displacement towards the companion such as might be expected if the companion galaxy was actively forming stars at a high rate.

It is clear from these results that PKS2250-41 is not a case of a source triggered in the final stages of a major galaxy merger. However, the scenario wherein a luminous AGN has been triggered by an encounter with another galaxy, some time after the point of closest approach, is far more plausible. Neither the radio galaxy nor its companion can be classed as a very massive elliptical. Additionally, the lack of very powerful far-IR emission from either source is consistent with low levels of starburst activity, with the AGN being the dominant cause of dust heating. If this is a case of triggering following a (first pass) galaxy encounter, the companion galaxy would most likely be on a highly elliptical orbit, and eventually merge with the radio source host at a much later point in time. Many of the different merger models predict relatively low levels of star formation until the nuclei finally merge (e.g. Hernquist & Mihos 1995, Springel et al 2005). The tidal forces associated with the initial encounter could be expected to cause the formation of the filamentary spur, while gas settling onto the central black hole for some time after the time of closest approach could trigger the AGN activity. Similar features are observed in the case of PKS0349-27 (Danziger et al 1984), which displays a tidal bridge linking it to a companion galaxy.

It is also interesting to contrast the results for PKS2250-41 with those of the $z=0.23$ FR II radio galaxy PKS1932-464 (Inskip et al 2007), which, like PKS2250-41, exists within an interacting group environment and also displays a spectacular EELR. However, the similarities end there. Despite the materially enriched IGM, the radio source of PKS1932-464

does not interact strongly with its environment. Additionally, while we observe little in the way of star formation associated with PKS2250-41, evidence for significant star formation is seen in the IGM surrounding PKS1932-464, as well as within the neighbouring companion galaxy. These results illustrate that even when AGN are triggered under apparently similar circumstances, a diversity of different outcomes are possible.

5 CONCLUSIONS

We have carried out a multiwavelength study of the radio source PKS2250-41, for the first time combining imaging, long-slit and IFU spectroscopic observations of this source. In addition to analysing the EELR in greater detail, we have now also been able to constrain the nature of the companion objects surrounding the host galaxy, as well as the nature of the host galaxy itself. This has allowed us to produce a far clearer picture of the different astrophysical processes ongoing within this source, and how the activity was triggered.

The key results are as follows:

- Our VIMOS IFU data produce results which are consistent with previous long-slit spectroscopy, allowing us to trace the different kinematic components across the EELR and confirming the effects of the jet-cloud interactions occurring within this source. We observe lower ionization level for the gas and broader lines in the vicinity of the western hotspots than elsewhere within the EELR, consistent with the presence of shocks in those regions. The remainder of the EELR gas is predominantly photoionized. In terms of the gas kinematics, we detect a north-south velocity gradient across the EELR and boosting of the line widths along the radio axis, particularly close to the western lobe hotspots. Narrower line emission is observed between the radio galaxy and the companion galaxy to the northeast.
- The host galaxy is an $\sim 1.4M_{\star}$ elliptical, and part of a group of galaxies, including a disk galaxy of the same redshift to the north-east, and a faint companion object currently interacting with the radio source in the vicinity of the western lobe secondary hotspot.
- Our detection of this faint companion object in the infrared allows us to constrain its SED. The recent star-formation implied by this result suggests that jet-induced star formation is indeed occurring within this object.
- The filamentary structure extending to the north east outwards from the host galaxy is potentially linked with the triggering of the current AGN activity in this source. We believe that a tidal encounter with the companion object is the most likely cause of the triggering of the activity.

This object provides some of the best evidence that radio source activity can be triggered in a tidal encounter with a companion, before the final merger, but after the first pass of the nuclei in interacting galaxies. PKS2250-41 is clearly a most remarkable object, and a showcase for many aspects of radio source physics. But perhaps its greatest advantage is its ability to further our understanding of both the triggering of radio source activity, and also of the influence that a radio source has on the material in its surrounding environment.

ACKNOWLEDGEMENTS

KJI acknowledges support from a PPARC research fellowship and JH a PPARC PDRA. The work of MV-M has been supported by the Spanish Ministerio de Educación y Ciencia and the Junta de Andalucía through the grants AYA2004-02703 and TIC-114. The IFS data published in this paper have been reduced using VIPGI, designed by the VIRMOS Consortium and developed by INAF Milano; KJI would particularly like to thank Paolo Franzetti for guidance in the use and reliability of the VIPGI software. We also thank the ESO technical and support staff for indulging our request for the use of SOFI in the small field mode. This research has made use of the NASA/IPAC Extragalactic Database (NED) which is operated by the Jet Propulsion Laboratory, California Institute of Technology, under contract with the National Aeronautics and Space Administration. We thank the anonymous referee for some very useful comments which greatly improved the clarity of this paper.

REFERENCES

- Appenzeller I., et al., 1998, *The Messenger*, 94, 1
 Barnes J.E., Herquist L., 1996, *ApJ*, 471, 115
 Baum S.A., Heckman T., van Breugel W., 1990, *ApJS*, 74, 389
 Best P.N., Röttgering H. J. A., Longair M. S., 2000, *MNRAS*, 311, 23
 Best P. N., Longair M. S., Röttgering H. J. A., 1997, *MNRAS*, 286, 785
 Bicknell G. V., Sutherland R. S., van Breugel W. J. M., Dopita M. A., Dey A., Miley G. K., 2000, *ApJ*, 540, 678
 Binette L., Wilson A. S., Storchi-Bergmann T., 1996, *A&A*, 312, 365
 Blanco V. M., Graham J. A., Lasker B. M., Osmer P. S., 1975, *ApJ*, 198, L63
 Bremer M. N., Fabian A. C., Crawford C. S., 1997, *MNRAS*, 284, 213
 Brodie J., Königl A., Bowyer S., 1983, *ApJ*, 273, 154
 Cardelli J. A., Clayton G. C., Mathis J. S., 1989, *ApJ*, 345, 245
 Chambers K. C., Miley G. K., van Breugel W. J. M., 1987, *Nature*, 329, 604
 Clark N. E., Tadhunter C. N., Morganti R., Killeen N. E. B., Fosbury R. A. E., Hook R. N., Siebert J., Shaw M. A., 1997, *MNRAS*, 286, 558
 Croft S., et al, 2006, *ApJ*, 647, 1040
 Danziger I. J., Fosbury R. A. E., Boksenberg A., Goss W. M., Bland J., 1984, *MNRAS*, 208, 589
 Dey A., van Breugel W., Vacca W. D., Antonucci R., 1997, *ApJ*, 490, 698
 Dickson R., Tadhunter C., Shaw M., Clark N., Morganti R., 1995, *MNRAS*, 273, L29
 Di Matteo T., Springel V., Hernquist L., 2005, *Nature*, 433, 604
 Dopita M. A., Sutherland R. S., 1996, *ApJS*, 102, 161
 Fragile P. C., Murray S. D., Anninos P., van Breugel W., 2004, *ApJ*, 604, 74
 Graham J. A., Price R. M., 1981, *ApJ*, 247, 813
 Groves B. A., Dopita M. A., Sutherland R. S., 2004a, *ApJS*, 153, 9
 Groves B. A., Dopita M. A., Sutherland R. S., 2004b, *ApJS*, 153, 75
 Heckman T. M., Smith E. P., Baum S. A., van Breugel W. J. M., Miley G. K., Illingworth G. D., Bothun G. D., Balick B., 1986, *ApJ*, 311, 526
 Hernquist L., Mihos J. C., 1995, *ApJ*, 448, 41
 Holt J., Tadhunter C. N., González-Delgado R. M., Inskip K. J., Rodríguez J., Emonts B. H. C., Morganti R., Wills K. A., 2007, *MNRAS*, 381, 61
 Howarth I. D., 1983, *MNRAS*, 203, 301
 Humphrey A., Villar-Martín M., Fosbury R., Vernet J., di Serego Alighieri S., 2006, *MNRAS*, 369, 1103
 Inskip K. J., Tadhunter C. N., Dicken D., Holt J., Villar-Martín M., Morganti R., 2007, *MNRAS*, 382, 95
 Inskip K. J., Best P. N., Longair M. S., Röttgering H. J. A., 2005, *MNRAS*, 359, 1393
 Inskip K. J., Best P. N., Röttgering H. J. A., Rawlings S., Cotter G., Longair M. S., 2002c, *MNRAS*, 337, 1407
 Inskip K. J., Best P. N., Rawlings S., Longair M. S., Cotter G., Röttgering H. J. A., Eales S., 2002b, *MNRAS*, 337, 1381
 Inskip K. J., Best P. N., Longair M. S., MacKay D. J. C., 2002a, *MNRAS*, 329, 277
 Jackson N., Tadhunter C., Sparks W. B., 1998, *MNRAS*, 301, 131
 Le Fèvre O., et al, 2003, *SPIE*, 4841, 1670
 McCarthy P. J., van Breugel W., Spinrad H, Djorgovski S., 1987, *ApJ*, 321, L29
 Mellema G., Kurk J. D., Röttgering H. J. A., 2002, *A&A*, 395, L13
 Mihos, J. C., Hernquist L., 1996, *ApJ*, 464, 641
 Moorwood A., Cuby J. G., Lidman C. 1998, *The Messenger*, 91, 9
 Moy E., Rocca-Volmerange B., 2002, *A&A*, 383, 46
 Nipoti C., Binney J., 2005, *MNRAS*, 361, 428
 Oosterloo T. A., Morganti R., 2005, *A&A*, 429, 469
 Persson S. E., Murphy D. C., Krzeminski W., Roth M., Rieke M. J., 1998, *AJ*, 116, 2475
 Rawlings S., Saunders R., 1991, *Nat*, 349, 138
 Sanders D. B., Mirabel I. F., 1996, *ARA&A*, 34, 749
 Sanders D. B., Soifer B. T., Elias J. H., Madore B. F., Matthews K., Neugebauer G., Scoville N. Z., 1988, *ApJ*, 325, 74
 Schiminovich D., van Gorkom J. H., van der Hulst J. M., Kasow S., 1994, *ApJ*, 423, L101
 Schlegel D. J., Finkbeiner D. P., Davis M., 1998, *ApJ*, 500, 525
 Scodreggio M., et al, 2005, *PASP*, 117, 1284
 Shaw M., Tadhunter C., Dickson R., Morganti R., 1995, *MNRAS*, 275, 703
 Simpson C., 1998, *MNRAS*, 297, L39
 Springel V, Di Matteo T, Hernquist L., 2005, *MNRAS*, 361, 776
 Stockton A., Canalizo G., Fu H., Keel W., 2007, *ApJ*, 659, 195
 Sutherland R. S., Bicknell G. V., Dopita M. A., 1993, *ApJ*, 414, 510
 Tadhunter C. N., Dicken D., Holt J., Inskip K., Morganti R., Axon D., Buchanan C., González Delgado R., Barthel P., van Bemmel I., 2007, *ApJL*, 661, 13
 Tadhunter C. N., Robinson T. G., González Delgado R. M., Wills K., Morganti R., 2005, *MNRAS*, 356, 480
 Tadhunter C. N., Dickson R., Morganti R., Robinson T. G., Wills K., Villar-Martín M., Hughes M., 2002, *MNRAS*, 330, 977
 Tadhunter C. N., Packham C., Axon D. J., Jackson N. J., Hough J. H., Robinson A., Young S., Sparks W., 1999, *ApJ*, 512, 91
 Tadhunter C. N., Morganti R., Robinson A., Dickson R., Villar-Martín M., Fosbury R. A. E., 1998, *MNRAS*, 298, 1035
 Tadhunter C., Shaw M., Clark N., Morganti R., 1994, *A&A*, 288, L21
 Tadhunter C. N., Fosbury R. A. E., Quinn P. J., 1989, *MNRAS*, 240, 225
 Taylor M. D., Tadhunter C. N., Robinson T. G., 2003, *MNRAS*, 342, 995
 Tilak A., O'Dea C. P., Tadhunter C., Wills K., Morganti R., Baum S. A., Koekemoer A. M., Dallacasa D., 2005, *AJ*, 130, 2513
 van Breugel W., Filippenko A. V., Heckman T., Miley G., 1985, *ApJ*, 293, 83
 Villar-Martín M., Tadhunter C., Morganti R., Axon D., Koekemoer A., 1999, *MNRAS*, 307, 24
 Willott C. J., Rawlings S., Jarvis M. J., Blundell K. M., 2003, *MNRAS*, 339, 173

Wills K. A., Tadhunter C., Holt J., González-Delgado R., Inskip
K. J., Rodríguez Zaurín J., Morganti R., 2007, MNRAS, in
press
Zanichelli A., et al, 2005, PASP, 117, 1271

APPENDIX A: EMISSION LINE FLUXES FROM THE FORS1 SPECTROSCOPY

Here we present the emission line fluxes from the 1.6 arcsec apertures extracted from our FORS1 long slit spectroscopic observations.

Table A1. Spectroscopic properties of PKS2250-41, determined from spectra extracted in successive $1.6''$ apertures across the slit. The total integrated line fluxes are given in units of $10^{-17}\text{erg s}^{-1}\text{cm}^{-2}$. Non-detected lines (denoted by a dash) would have a maximum flux of the order of $1 \times 10^{-17}\text{erg s}^{-1}\text{cm}^{-2}$. Errors are dominated by flux-calibration errors (estimated to be $\lesssim 10\%$); the listed error values are determined by adding this calibration error in quadrature with the errors arising from photon statistics. All quoted values in this table are corrected for galactic extinction using the $E(B - V)$ for the Milky Way (Schlegel, Finkbeiner & Davis 1998) and the empirical extinction function of Cardelli et al (1989).

Spectrum:	Redshift	[SII] 4072Å	H δ 4102 Å	H γ 4340Å	[OIII] 4363Å	HeII 4686Å	H β 4861Å	[OIII] 5007Å
S1: $-6.4''$	0.3083	–	–	–	–	–	3.97 ± 0.96	39.64 ± 4.02
S2: $-4.8''$	0.3083	–	4.69 ± 1.18	9.90 ± 1.44	< 1.67	–	16.59 ± 1.98	90.45 ± 9.09
S3: $-3.2''$	0.3081	–	–	3.88 ± 0.99	< 1.94	–	7.18 ± 1.40	32.85 ± 3.42
S4: $-1.6''$	0.3082	–	–	4.92 ± 1.10	< 2.46	–	13.01 ± 1.80	96.98 ± 10.00
S5: $+0.0''$	0.3076	4.37 ± 0.95	14.36 ± 1.98	27.58 ± 3.15	15.43 ± 2.19	19.74 ± 2.24	62.29 ± 6.34	696.22 ± 69.74
S6: $+1.6''$	0.3073	–	10.24 ± 1.54	22.41 ± 2.52	10.78 ± 1.44	14.24 ± 1.70	46.80 ± 4.80	551.08 ± 55.25
S7: $+3.2''$	0.3076	–	–	3.62 ± 0.92	–	–	3.87 ± 1.32	37.14 ± 3.84
S8: $+4.8''$	0.3077	–	–	–	–	–	1.33 ± 0.64	7.76 ± 1.02
S9: $+6.4''$	0.3076	–	–	–	–	–	–	3.16 ± 0.72
S10: $+8.0''$	0.3074	–	–	–	–	–	–	10.06 ± 1.25
S11: $+9.6''$	0.3084	–	–	–	–	–	–	2.25 ± 0.76